Winiberg, F. A. F., Percival, C. J., Shannon, R., Khan, A., Shallcross, D., Liu, Y., & Sander, S. P. (2018). Reaction Kinetics of OH + HNO_3 under conditions relevant to the Upper Troposphere/Lower Stratosphere. *Physical Chemistry Chemical Physics*, *20*, 24652-24664. https://doi.org/10.1039/C8CP04193H

Reaction Kinetics of OH + HNO_3 under conditions relevant to the Upper Troposphere/Lower Stratosphere

Frank A. F. Winiberg[1], Carl J. Percival[1], Robin Shannon[2,3], M. Anwar H. Khan[2], Dudley E. Shallcross[2], Yingdi Liu[1], Stanley P. Sander[1]

[1] NASA Jet Propulsion Laboratory, California Institute of Technology, Pasadena, CA 91109, USA

[2] School of Chemistry, Cantock's Close, University of Bristol, Bristol, BS8 1TS, UK

[3] Department of Mechanical Engineering, Stanford University, 452 Escondido Mall, Stanford, CA 94305, USA;

Corresponding Authors

*Stanley P. Sander. Phone: 1-818-354-2625. Fax: 1-818-393-5019.

E-mail: Stanley.Sander@jpl.nasa.gov.

ABSTRACT

The OH initiated oxidation of HNO_3 in the UT/LS plays an important role in controlling the O_3 budget, removing HO_x radicals whilst driving $NO_{x/y}$ partitioning chemistry by yielding NO_3 radicals.

$$OH + HNO_3 \rightarrow H_2O + NO_3 \quad (1)$$

In this paper, k_1(T, P) was measured using OH ($A \leftarrow X$) Laser Induced Fluorescence (LIF) and the data was modelled over the 220 – 300 K temperature and 25 – 750 Torr pressure ranges, using the modified Lindemann-Hinshelwood expression $k_1 = k_0 + \frac{k_3[M]}{1+\frac{k_3[M]}{k_2}}$, where k_0 = 5.20 × 10^{-14} exp(199/T) cm^3 s^{-1}, k_2 = 8.39 × 10^{-14} exp(1921/T) cm^3 s^{-1} and k_3 = 1.60 × 10^{-14} exp(1745/T) cm^3 s^{-1}. A significant source of experimental uncertainty derives from accurate determination of HNO_3 concentration, which is impacted by heterogeneous uptake of the low volatility HNO_3 onto cold surfaces of the reactors. Our results represent the determination of k_1(T, P) using two different *in-situ* [HNO_3] measurements: VUV absorption and a new two photon Photolysis Induced Fluoresence (PIF). Experimental results are discussed along with a computational master equation calculation (MESMER), which highlight the need for further theoretical study into the OH + HNO_3 mechanism and potential energy surface. The atmospheric impact of these new rate constants were modelled using the STOCHEM-CRI chemistry transport global model, which have shown a small reduction in global budgets of key atmospheric species, with more significant changes in the NO_x/HNO_3 ratio, peaking in the tropical upper troposphere regions

1 Introduction

Nitric acid (HNO_3) is one of the termination products for NO_x (=NO + NO_2) and most abundant nitrogen-containing species in our atmosphere. The removal processes for HNO_3 vary with altitude and even latitude. In the lower troposphere dry and wet deposition dominate the loss of HNO_3, but, in the upper troposphere/lower stratosphere (drier and colder parts of the atmosphere), HNO_3 is longer lived, and thus can be removed by OH initiated oxidation of HNO_3.

$$OH + HNO_3 \rightarrow H_2O + NO_3 \quad (1)$$

Reaction (1) plays an important role in controlling the O_3 budget. HNO_3 is produced from the reaction of OH with NO_2 (reaction (2)), and the oxidation product, NO_3 from the reaction (1), drives $NO_{x/y}$ partitioning chemistry (where NO_y = NO + NO_2 + NO_3), ultimately recovering NO_2 (reactions (3-4))

$$OH + NO_2 \rightarrow HNO_3 \quad (2)$$

$$NO_3 + hv \rightarrow O + NO_2 \quad (3)$$

$$HO_2 + O_3 \rightarrow OH + 2O_2 \quad (4)$$

$$O_2 + O \rightarrow O_3 \quad (5)$$

$$\textbf{Net: } OH + HO_2 \rightarrow H_2O + O_2 \quad (6)$$

Accurately quantifying the rate coefficient k_1 as a function of temperature and pressure is therefore critical for prediction of the O_3, HO_x, and NO_x budgets in the UT/LS. However, at present models do not accurately describe the observed nitrogen partitioning, in particular, under-predicting the ratio of NO_x/HNO_3 [1-3]. HNO_3 is an important reservoir for NO_2, producing O_3 by photolysis in the

lowermost stratosphere and catalyzing O_3 destruction at higher altitudes. In the UT/LS region, models are if anything under-predicting the *in-situ* production of ozone. Several theories have emerged to explain the model discrepancy, including a variety of heterogeneous processes such as the reduction of HNO_3 on black carbon [4]. At present no single theoretical proposal has provided a solution to model under-prediction of NO_x/HNO_3. Brown, *et al.*,[5] have shown that the reaction of HNO_3 with OH is faster than previously measured. Gao, *et al.*,[6] and Lary, *et al.*,[7] have observed that these new kinetic data improve the agreement between model and measurements in the lower stratosphere and troposphere respectively, but that discrepancies still exist which must be addressed.

There have been four experimental studies of rate coefficients for the reaction of OH with HNO_3 as a function of temperature and pressure: Margitan and Watson,[8] over the pressure range of 20 – 100 Torr and temperature range of 225- 415 K, Stachnik, *et al.*,[9] over the pressure range of 10 – 730 Torr and at two temperatures of 248 and 297 K, Brown, *et al.*,[5] between 50 and 500 Torr over the temperature range of 200-375 K and the most recent study by Dulitz, *et al.*,[10] over the pressure range of 18 – 696 Torr and the temperature range of 208 – 318 K. The three earlier studies are in fair agreement which led to the current JPL recommended uncertainty in k_1 of 20% ($\pm 1\sigma$) at STP. However, under UT/LS conditions (low T and P), the uncertainty could increase to as much as ± 50%. The uncertainty in rate constant translates to 10 - 20% in model predictions of NO_x/NO_y partitioning. Indeed, in a recent study on the impact of uncertainty in rate constants on tropospheric composition it was shown that the uncertainty of k_1 has a significant impact on modelled O_3 [11].

All previous studies have been performed under pseudo first order conditions and require accurate determination of HNO_3 concentration in order to convert experimentally observed decay constants into bimolecular rate coefficients. Until recently [10], former studies have relied on *ex-situ*

measurements of the HNO_3 concentration after the reaction cell, which could lead to greater uncertainties in the overall determination of the rate coefficient from heterogeneous uptake of the low volatility HNO_3 onto cold surfaces of the reactors used. The work by Dulitz, *et al.*,[10] utilizes a two-photon photolysis induced fluorescence detection method for HNO_3 and has shown that at low temperatures k_1 may be smaller than previously thought. Photolysing the HNO_3 and measuring fluorescence in the center of the reactor allows a more accurate determination of [HNO_3] in the kinetic measurement region (i.e. *in-situ*). In the results presented here, we employ an alternative photolysis based fluorescence method of HNO_3 characterization to study k_1 over the 50 – 750 Torr pressure range and 223 – 298 K temperature range.

2 Experimental

2.1 PLP-LIF apparatus

The Pulsed Laser Photolysis-Laser Induced Fluorescence (PLP-LIF) apparatus has been described in detail previously [12, 13] and a diagram is displayed in Figure 1. The circular, stainless-steel, 4-axis cell was designed to allow the laser beams from a high energy KrF excimer laser and the output of a frequency doubled YAG-pumped dye laser to overlap at right angles, whilst providing an additional axis for gas flow and a final axis for reactant concentration determination (see section 2.2).

Mass flow controllers (MKS) were used to control the flow of gas into the cell, and the desired bath gas pressure (25 – 750 Torr) was maintained using a 1000 Torr pressure gauge (MKS 627B) combined with an automated valve and pressure controller (MKS 120 Series). Reactants were mixed with N_2 bath gas in a 5-port glass manifold ~50 cm before entering the cell. Flow rates were

chosen so that the residence time in the photolysis region was ~50 ms, ensuring a new gas sample was probed with each photolysis laser shot.

The cell was cooled using an internally mounted copper shroud coated with amorphous Teflon®. Cold methanol was circulated around the shroud using a home-built liquid nitrogen (LN_2) based circulator system. LN_2 was flowed through a coil submerged in the methanol bath and controlled by a solenoid valve connected to an Omega PID controller (Cn8i). The temperature of the bath and coolant input line was monitored by the controller, allowing the reaction cell to be controlled between 223 – 273 K at ± 1 K. Cell temperatures were monitored in the gas outflow, close to the reaction volume using a K-type thermocouple and Ultra-Torr feedthrough.

The OH radicals were generated by photolysis of HNO_3 at 248 nm using an Excimer laser (LPX 120i, Lambda Physik) operating at 20 Hz repetition frequency:

$$HNO_3 + h\nu\,(248\text{ nm}) \rightarrow OH + NO_2 \qquad (7)$$

The ~10^{10} OH radicals cm^{-3} produced reacted with the excess of HNO_3 in the system ($[HNO_3] \approx [OH] \times 1000$) under pseudo first-order kinetic conditions.

The decay of the OH radicals was monitored using LIF, exciting OH in the $A^2\Sigma \leftarrow X^2\Pi$ ($v' = 1$, $v = 0$), $Q_{11}(1)$ transition at 281.997 nm and measuring the emission at 308 ± 5 nm ($A^2\Sigma \rightarrow X^2\Pi$, $v' = 0$, $v = 0$). The 282 nm light was produced from the frequency doubled output of a diode pumped, solid state YAG laser (YHP340 DPSS) pumping a dye laser (Sirah Cobra Stretch using Rhodamine 6G) operating at 20 kHz repetition frequency. The fluorescence at 308 nm was collected onto a PMT (Senstec) using a concave back-reflector, two collimating/focusing optics and a series of baffles. The collimated fluorescence was passed through a narrow band pass filter (308 ± 5 nm, Barr Associates) to discriminate from the 282 and 248 nm laser pulses.

The discriminated pulses from the PMT were photon counted using a multichannel scaler (Ortec, MCS pci) and the two lasers and photon counting system were triggered using a BNC delay generator (Berkeley Nucleonics 535). Setting the MCS bin width to 50 μs (the time delay for each 282 nm pulse) allows for a 1000 data point kinetic profile for the OH decay to be measured for each photolysis laser pulse (20 Hz). OH decay profiles were measured over 6 – 10 concentrations of HNO_3 for a given temperature and pressure. The observed decays were fit with a single exponential function to derive the pseudo-first order rate coefficient, k'. Plotting the observed k' as a function of [HNO_3] allowed k_1 to be determined, as $k' = k_1[HNO_3]$.

Gas phase HNO_3 was introduced into the cell by flowing 3 – 100 sccm of N_2 through a bubbler containing a 1:3 mixture of HNO_3 (70% in H_2O) and H_2SO_4 (conc.). There is the possibility of impurities arising from the HNO_3 source, which could interfere with the determination of k_1, increasing the measured pseudo-first order rate coefficient. These include N_2O_4, N_2O_5 and NO_2 (from the thermal decomposition of HNO_3). The production of significant [NO_2] from the HNO_3 source was mitigated by bubbling the bath gas through the bubbler for 20 - 30 minutes prior to starting an experiment. The absence of NO_2 in the reaction cell was confirmed using a 50 cm *ex-situ* absorption cell coupled to a quartz halogen lamp and spectrograph with CCD (Acton 300i and Princeton Instruments PIXIS 100). Based on the [HNO_3] produced during this test (~4×10^{15} cm^{-3}) and the NO_2 limit of detection of the apparatus (~5×10^{12} cm^{-3}), the [NO_2] upper limit was established to be < 1%. Based on this measurement and using the maximum $k_{(OH+NO2)}$ (= 2×10^{-11} cm^{-3} at 220 K, 750 Torr), an upper limit of ~10% uncertainty in k_1 of $k_{(OH+NO2)}$ on the k_1 determination was estimated.

2.2 HNO_3 detection

Two methods were used for the detection of HNO_3 in this work. In the first instance, direct vacuum ultraviolet (VUV) absorption at 185 nm both *in-situ* and *ex-situ* was used to quantify the HNO_3 concentration. In the second, a newly developed two-photon based (λ = 248 nm) Photolysis Induced Fluorescence (PIF) method of HNO_3 detection was used (described in detail in a future publication)[14].

2.2.1 VUV absorption – 185 nm

HNO_3 was detected using VUV absorption at 185 nm both *in-situ* and *ex-situ*. The *in-situ* measurement was made at 90 degrees to the gas flow axis, using 1" diameter glass inserts to constrain the measurement pathlength to the inside of the copper shroud. Constraining the pathlength in this manner reduced the likelihood of measuring reactant concentration gradients across the reaction cell diameter. The glass inserts were positioned ~1 cm from the wall of the shroud, leading to a pathlength of 10.9 cm (shroud diameter = 13.2 cm). The glass inserts were open on the chamber side, sealed externally with Suprasil windows. A glass valve allowed the arms to be purged continuously using N_2 to mitigate the condensation of HNO_3 onto the absorption cell axis surfaces (the purge method is discussed in greater detail in the supplementary information). The *ex-situ* absorption measurement cell had a diameter of 2.5 cm, 50 cm length and was positioned after the reaction cell (see Figure 1).

Both absorption cells used the 185 nm output of an Hg-Ar penray lamp (LOT-Oriel) combined with Suprasil windows to maintain vacuum and three narrow-bandpass filters (LOT-Oriel, (185 ± 10) nm (FWHM)) to exclude the longer wavelength emissions from the Hg lamp. Light was detected using a photomultiplier tube (PMT, LOT-Oriel, Ar-Hg). For the *ex-situ* method, all three filters were placed directly in front of the PMT and for the *in-situ* absorption path, two filters were

placed directly after the Hg lamp and one filter was placed in front of the PMT. The two filters before the reaction cell limited the weak Hg lamp emission at ~312 nm from interfering with the simultaneous LIF data collection cycle. The path lengths of the *in-situ* and *ex-situ* absorption cells were characterized using a combination of static and flow experiments. The path length determinations are discussed in more detail in the supplementary information.

The absorption cross-section for HNO_3 at 185 nm, σ_{185nm}, has been determined several times in the literature [15-17]. More recently, Dulitz, *et al.*,[10] have confirmed the previous measurements using a meticulous apparatus to account for a variety of impurities (NO_2, NO_3, N_2O_5, and H_2O) and measure at two wavelengths simultaneously. Based on these studies, $\sigma_{185nm} = (1.6 \pm 0.1) \times 10^{-17}$ cm^2 was used here.

2.2.2 HNO_3 Photolysis Induced Fluorescence (PIF)

The *in-situ* absorption method suffers from possible reagent concentration gradients across the cell diameter, and the *ex-situ* method suffers from possible under-determination of the [HNO_3] as a result of heterogeneous uptake of the HNO_3 onto the cell walls. To compensate for this problem, HNO_3 characterization using 2-photon photolysis was implemented.[10, 14, 18] Briefly, the 248 nm output of the excimer laser was focused into the center of the reaction cell (UV-fused silica plano-convex, f = 1000 mm). When a molecule of HNO_3 was pumped with two photons of 248 nm light, fluorescence was observed at ~308 nm from the photodissociation products. Our sister publication has identified the emissions as a combination of short-lived OH ($A \rightarrow X$) fluorescence and longer lived NO ($A \rightarrow X$) fluorescence (t ~30 μs)[14]. Spectral identification experiments in a future complementary publication[14], where higher energy NO ($A \rightarrow X$) transitions between $v'' = 0 - 3$ were responsible for the observed emissions around 308 nm. Whilst the emissions from OH occur

on very short timescales (t ~100 ns), too close to the excimer laser pulse to deconvolve from scattered light and PMT saturation, the longer-lived NO emission can be monitored using the same PMT/Filter/MCS combination as the OH LIF detection system. The NO ($A \rightarrow X$) emission was monitored over the t_0 + 20 μs to t_0 + 200 μs range with 100 ns bin width. A strong dependence of the NO ($A \rightarrow X$) emission lifetime was observed with respect to [HNO_3] (~2×10^{-11} cm^3 s^{-1}), from the quenching of the NO excited state. Using a Stern-Volmer analysis, the lifetime of the NO ($A \rightarrow X$) emission was observed to decrease linearly with [HNO_3], enabling the calibration of the NO emission lifetime using the *ex-situ* VUV absorption measurement at 298 K for each pressure used in this study (25 – 750 Torr). An example decay fit and dependence of decay rate with respect to [HNO_3] conducted at 298 K and 200 Torr N_2 is shown in Figure S1. Before/after an OH LIF kinetic measurement at a given temperature and pressure, the NO ($A \rightarrow X$) emission lifetime was converted to [HNO_3] using the room temperature calibration. This method of [HNO_3] determination was cross-validated with the VUV absorption [HNO_3] determination at 273 and 253 K before extending the PIF method down to 223 K.

3 Results and discussion

3.1 k_1 determination

Experiments were conducted under pseudo-first order conditions with respect to the OH radicals. As [HNO_3] >> [OH], measurement of the exponential decay of OH allowed for the determination of k_1 by measuring the pseudo first order decay rate, k', over a range of [HNO_3]. Typically [HNO_3] = 0.1 – 5.0 $\times 10^{15}$ cm^{-3}. Displayed in Figure 2 are the OH decay profiles recorded at 200 Torr and 235 K ([HNO_3] = 0.3 – 1.4 $\times$ 10^{15} cm^{-3}), fit with a single exponential decay to determine k'. The

inset figure shows the rate coefficient determination for the same experiment by plotting k' against the [HNO_3] measured using the *in-situ* 2*hv* PIF method.

3.2 VUV/2*hv* [HNO_3] comparison

To validate the 2*hv* PIF method of HNO_3 detection, k_1 was measured using both the *in-situ* VUV absorption and PIF to characterize the [HNO_3], simultaneously, at 273 and 253 K. Displayed in Figure 3 are the observed rate coefficients measured over the 50 – 750 Torr pressure range. Each data point represents the weighted average of 3 or more measurements and the error bars represent the total uncertainty in the measured rate coefficient to ± 2σ. Excellent agreement was observed between the k_1 measured using the two methods at both temperatures, validating the 2*hv* PIF detection method and improving confidence in the performance at lower temperatures.

Attempts were also made to measure the [HNO_3] using the *ex-situ* VUV absorption cell. However, at temperatures < 298 K, discrepancies in the k_1 determined using the *ex-situ* VUV and *in-situ* VUV and 2*hv* PIF detection methods were observed. Figure 4 shows a comparison of a second order plot measured at 235 K and 200 Torr between the *ex-situ* method and the 2*hv* PIF detection method. It can be seen clearly that the concentrations measured *ex-situ* are systematically lower than those measured *in-situ*, increasing the measured rate coefficient and leading to negative intercepts. The *ex-situ* cell was located downstream of the LIF cell and thus we hypothesize that heterogeneous loss of the HNO_3 to the reactor walls occurred, leading the *ex-situ* cell to give an unrepresentative measure of [HNO_3]. Rate coefficients below 298 K were therefore calculated from a combination of the *in-situ* VUV absorption and the PIF methods at 273 and 250 K, and from the PIF method solely below 250 K.

3.3 k_1 (T,P)

Figure 5 shows the observed k_1 as a function of [N_2] (25 – 750 Torr) over the 223 – 298 K temperature range. Each data point represents the weighted average of 3 or more measurements and the error bars represent the total uncertainty in the measured rate coefficient to ±2σ. The experimental data shown here are displayed in Table 1, for reference. Uncertainties in k_1 (T, P) were calculated as the sum in quadrature of the precision of the bi-molecular rate coefficient fit combined with the systematic uncertainties outlined in Table 3. Fit precisions are listed with their respective rate coefficients in Table 1. The largest uncertainty in the k_1 (T, P) measurement are from the determination of the [HNO_3]. Based on the thorough studies of σ_{185nm} in the literature, which are in excellent agreement [10, 15-17], the recommended uncertainty of ± 6% was used. The uncertainty in the pathlength measurement for the VUV absorption method was measured for each pressure and temperature combination. Therefore, each T, P combination had an individual pathlength determination with a respective error, for which a systematic 2% uncertainty represents the upper limit for all pathlength determinations for the VUV derived k_1 measurements. Finally, there was a small systematic uncertainty in the temperature control method, to which we assign a 2% uncertainty. As all experiments were conducted using a pressure control valve to maintain a constant reactor pressure (0.1% accuracy), this systematic uncertainty was considered negligible. Due to the nature of both measurements relying on the σ_{185nm}, a 7% total systematic uncertainty was applied to all k_1 data points, irrespective of the [HNO_3] determination.

The rate coefficients obtained in this study agree very well with the current JPL parametrization at room temperature[19]. The parametrization assumes that OH reacts with HNO_3 to form a chemically activated, weakly bound complex, OH---HNO_3*. The complex can dissociate back to OH + HNO_3 (and is therefore in equilibrium with the reactants), or via a small barrier, OH---

HNO_3* can proceed to products, $NO_3 + H_2O$. However, if the excited complex undergoes collision with a bath gas partner, a more stabilized complex intermediate can be formed. Both the quenching and chemically activated product channels remove observable OH radicals (in these experiments). As the temperature in the system decreases, the average energy of the nascent complex decreases and therefore the quenching of the complex increasingly competes with unimolecular decomposition of the complex back to reactants and so the apparent rate constant for OH removal increases as T decreases. This OH removal process is enhanced at higher total pressures, where quenching becomes more significant. Work by Brown, *et al.*,[20] has shown through direct NO_3 measurements, that even upon stabilization, the complex is able to proceed to $NO_3 + H_2O$ products, with a branching ratio of 1. The likely hypothesis was through a tunneling mechanism. To describe this effect, Lamb, *et al.*,[21] used a modified Lindemann Hinshelwood expression, used by Brown, *et al.*,[5], as given in equation (I):

$$k_1 = k_0 + \frac{k_3[M]}{1+\frac{k_3[M]}{k_2}} \qquad \text{(I)}$$

where k_0 = low pressure (bimolecular) limit, $k_2 = k_\infty - k_0$ (where k_∞ = high pressure limit), and k_3 = concerted termolecular term for the two step formation of the stabilized OH---HNO_3 intermediate. The fitted parameters from equation (I) are given in Table 2, in comparison to the current JPL recommended rate coefficients. Whilst the agreement is good at room temperature, as the temperature decreases the rate coefficients obtained in this study are significantly smaller than the parameterization suggested by the current JPL evaluation Burkholder, *et al.*,[19] and Brown, *et al.*,[5]. Figure 5 also shows a global fit of these data obtained in this study using equation (I), for a direct comparison with the current JPL parameterization. In order to obtain the global fit of the fall off curve as a function of temperature, it is necessary to use low pressure rate coefficients obtained

by other studies. Figure 6 shows, all experimentally obtained rate coefficients at 10 Torr or below. Jourdain, *et al.*,[22], Connell and Howard,[17], and Devolder, *et al.*,[23] studied reaction (1) using the discharge flow technique and represent the only direct low-pressure determinations of the rate coefficients as a function of temperature. Figure 6 also includes the linear extrapolation from 20 Torr to 0 Torr of the flash photolysis studies reported by Margitan and Watson,[8], where the rate coefficient at zero Torr was assumed to be the low pressure limit. It is now well known that the fall off with pressure is not linear and the "0 Torr" rate constant should only be considered as an upper limit. The early flash photolysis studies of Wine, *et al.*,[16], Marinelli and Johnston,[24], and Kurylo, *et al.*,[25] were all studied at higher pressures; but within experimental error did not observe any pressure dependence. These studies are thus included in for completeness, but were not considered in the choice of low pressure rate constant for the fall-off curve fit, as the later experimental studies and recent theoretical results show that a pressure dependence of reaction (1) is observed. In Figure 6 there is considerable scatter in the kinetic database for the Arrhenius plot for reaction (1). The choice of the low pressure rate coefficients has a significant impact on the parameters obtained from equation (I). Of the three investigations at low pressure, Jourdain, *et al.*,[22] and Devolder, *et al.*,[23] estimated [HNO_3] purely in terms of flow dilution. However, as we have shown, this assumption is not valid, especially at low temperatures where there is significant loss of HNO_3 due to heterogeneous loss as the sample passes through the cooled reactor region. Furthermore, these studies were obtained using low pressure flow tube systems, where wall loss can be significant (e.g. Seeley, *et al.*,[26]). However, Connell and Howard,[17] independently measured the [HNO_3] using UV absorption after the flow tube. Therefore, the Arrhenius expression from Connell and Howard,[17] was used to calculate the low pressure rate coefficients used to fit the experimental data using equation (I), at the temperatures relevant to this study:

$k = (2.0 \pm 0.4) \times 10^{-14} \exp[(430 \pm 60/T)]$ cm^3 s^{-1}

It is interesting to note that the rate coefficients measured by Connell and Howard,[17] are lower than those obtained by Jourdain, *et al.*,[22] and Devolder, *et al.*,[23]; this would be expected if there was unaccounted HNO_3 loss along the cold flow tube. In a recent study, Dulitz, *et al.*,[10] also used the low pressure rate constants of Connell and Howard,[17] to fit the fall off of reaction (1), also noting that it was the only low pressure study that experimentally determined [HNO_3].

The fit to these data obtained in this study is shown in Figure 5 and the parameters from equation (I) are given in Table 2. It should be noted that Burkholder, *et al.*,[19] used the Devolder, *et al.*,[23] data to constrain the low-pressure limit of their fit. Figure 7 shows a direct comparison of the fit to our data, using equation (I), constraining the low pressure fit with both the Devolder, *et al.*,[23] and the Connell and Howard,[17] Arrhenius expressions. The uncertainties in the given Arrhenius expressions were used to weight the data fits. In Figure 7, at temperatures and pressures that are relevant to the UT-LS region (highlighted in red) the differences in rate coefficients are very small (within experimental error), thus the choice of low pressure rate coefficients will not have a significant impact for atmospheric modelling up to ~16 km. However, in the fall off region at lower pressures (for total [N_2] < 5×10^{18} cm^{-3}) the difference is significant. Future studies at low pressures are required in order to resolve this difference.

There have only been three studies of the pressure dependence of reaction (1) at temperatures below 250 K. Figure 8 shows a comparison of the fit parameters from this work with Brown, *et al.*,[5] and Dulitz, *et al.*,[10] calculated at 235 K using equation (I). All studies were carried out using flash photolysis systems with LIF detection of OH studied under pseudo first order conditions. Both this study and Dulitz, *et al.*,[10] use an *in-situ* method of [HNO_3] determination in an attempt

to minimize the impact of heterogeneous loss of HNO_3 in the LIF cell on the rate coefficient measurement. Similar to the rate coefficients reported in Dulitz, *et al.*,[10] this paper reports rate coefficients that are lower than those of Brown, *et al.*,[5], especially at low temperature, as shown in Figure 8. Brown, *et al.*,[5] compared the measured [HNO_3] using an *ex-situ* cell and *in-situ* across the LIF cell using UV absorption. Across all temperatures, they reported that both measurements agreed within 5% and thus only used the *ex-situ* measurement of [HNO_3] for rate coefficient determination. It remains unclear as to why there is a discrepancy in k_1 between this work and that of Brown, *et al.*,[5], however with our experimental system it was not possible to measure the [HNO_3] reliably at temperatures below 298 K using the *ex-situ* cell.

It is impossible to directly compare the rate coefficients obtained in this study with those of Dulitz, *et al.*,[10], as the experiments were not performed at identical temperatures. As can be seen in Figure 8 there is broad agreement between the two studies. However, within experimental error it seems that the rate coefficients reported by Dulitz, *et al.*,[10] are pressure independent at P > 50 Torr. This is in disagreement with Margitan and Watson,[8], Stachnik, *et al.*,[9] and Brown, *et al.*,[5]. Figure 8 also shows a comparison of the fall off curves reported by JPL evaluation 15-10 [19], Dulitz, *et al.*,[10] and this study. Dulitz, *et al.*,[10] have suggested that, within error, they agree with the Brown, *et al.*,[5]. However, as can be seen in Figure 8, there is a significant difference between the experimentally obtained rate coefficients of Dulitz, *et al.*,[10] and those of Brown, *et al.*,[5] which would explain the non-negligible difference in modelled [HNO_3] in the UT-LS reported in their publication. It is unclear why the fall off curve reported by Dulitz, *et al.*,[10] and that reported in this work are different in shape, as there is broad agreement between the two studies. However, we incorporate the errors reported by Connell and Howard,[17] in the global fit to equation (I) and it is unclear if Dulitz, *et al.*,[10] also weight their fit to include the experimental error in the low-pressure rate coefficients.

3.4 Master Equation Simulations

In order to complement the experimental results, statistical rate theory calculation have been performed for the OH + HNO_3 system in the form of the energy-grained master equation (EGME) [27-29]. Such EGME approaches have become a standard tool for interrogating the kinetics of systems involving one or more intermediates or potential wells.

Before performing EGME simulations it is necessary to characterize the stationary points of the OH + HNO_3 potential energy surface (the bound and transition states) using electronic structure theory. There have been two previous theoretical studies of the OH + HNO_3 system by Xia and Lin,[30] and Gonzalez and Anglada,[31]. These previous works display substantial variation in the calculated energies and barrier heights. In particular Gonzalez and Anglada,[31] have performed particularly comprehensive calculations and find large variations in energies depending upon the method used to optimize the stationary points. In this work all stable species and transition states were optimized at the M06-2x / 6-311+G(3d,2p) level of theory using the Gaussian09 [32] suite of electronic structure codes. An ultrafine integration grid was used for these calculations. At these optimized geometries ROHF-CCSD(T)-f12/aug-cc-pVTZ [33] single point calculations were performed using the MOLPRO package [34]. A schematic potential surface is shown in Figure 9.

Both previous studies found multiple conformers for both the pre-reaction complex IM1 and the transition state TS1. We also find two distinct conformers at the B3LYP/6-311+G(3d,2p) level of theory, but we cannot identify the second conformer at the M06-2x / 6-311+G(3d,2p) level of theory. All other conformers are related by internal rotations and as such they are more properly considered by utilizing a hindered rotor treatment. The energies of IM1 and TS1 in the current work agree well with previous calculations from Gonzalez and Anglada,[31] and Xia and Lin,[30] though there is substantial variation in the energy of TS2.

In addition to the single point analysis we also performed electronic structure calculations to evaluate torsional potentials for the inter-moiety hindered rotations in IM1 and TS1. Constrained geometry optimizations were performed at the M06-2x/6-31+G* level of theory keeping the dihedral angles corresponding to the torsional motions fixed. The bonds / H-bonds around which rotation was considered are shown in the Figure S1 of the online supporting information and these scans consisted of 30 degree increments of the dihedral angle between 0 and 360 degrees. Similar calculations were performed for rotation about the central bond of HNO_3. All potentials can be found in the example MESMER input file in the supporting information

With the potential energy information above it was then possible to perform EGME simulations with the open source master equation software MESMER [35]. These simulations utilized the potential energy surface shown in Figure 9 incorporating hindered rotational potentials for the torsions described. The EGME used here has been described in detail previously [27-29]. Briefly, the EGME treats the kinetics of the system at the micro-canonical (energy resolved level) and considers the competition between chemical reaction and energy transfer with the system bath. Micro-canonical rate coefficients are typically obtained from RRKM theory and energy transfer properties for all wells are calculated assuming an exponential down model parameterized by the average energy transferred upon collision with the bath ($\langle \Delta E_{down} \rangle$). For the barrierless reaction forming IM1 from HNO_3 + OH, variational approaches would usually be necessary to calculate the micro-canonical rate coefficients for this process from first principles. Such variational calculations require large amounts of accurate potential energy information and for the current case we have chosen instead to treat this barrierless process using an inverse Laplace transform (ILT) method [36]. In this method, given a rate expression for the high pressure limiting canonical rate coefficients (k(T)'s) for this system, an inverse Laplace transform is used to obtain the

microcanonical k(E)'s required in the EGME analysis. Such barrierless processes typically have high reaction probabilities with rate coefficients close to the capture limit on the order of 1×10^{-10} cm^3 s^{-1}. In the current case we have assumed a temperature independent k(T) for the ILT expression and it is found that the overall phenomenological rate coefficients for the system are insensitive to the value of k_1(T) between values of 3×10^{-10} cm^3 s^{-1} and 1×10^{-11} cm^3 s^{-1}. Previous proxy method experiments by McCabe, *et al.*,[37] on the OH + HNO_3 give a rate coefficient of 2.5×10^{-11} cm^3 s^{-1} for OH(v=1) + HNO_3. This should provide a good lower limit to the true high pressure limiting rate coefficient for OH + HNO_3 and as such we have chosen to use a temperature independent high pressure k_1(T) of 2.5×10^{-11} cm^3 s^{-1} for the ILT used in the current work.

Molecular ro-vibrational densities of states were obtained for all species assuming rigid-rotor, harmonic oscillator behavior apart from the large amplitude torsional modes in IM1 and TS1, which were modeled as a hindered rotor subject to the potential described earlier. The torsional motion was then projected from the hessian to obtain a new set of harmonic vibrations according to the method of Sharma, *et al.*,[38] as implemented in MESMER. For the hydrogen transfer process from IM1 to IM2 quantum mechanical tunneling was treated assuming an asymmetric Eckhart barrier parameterized by the imaginary frequency of the transition state. This is an approximation to the true vibrationally adiabatic reaction path subject to tunneling, however since in the current work the EGME simulations are being fit to experiment, this tunneling model has the advantage of relying upon only a single parameter, which can be varied in order to fit to experimental rate coefficients. The MESMER input used in the current work is given in the supplementary information. It is noted that the MESMER input does not include the final bimolecular products H_2O + NO_3 since it was found under all conditions that once IM2 was formed the reaction proceeded directly to these products. IM2 was treated as an infinite sink to reflect this.

Given the large array of experimental data available for this system we have tuned some of the EGME parameters in order to fit the experiment. The parameters fit are the imaginary frequency and barrier height of TS1 and the $\langle \Delta E_{down} \rangle$ values for IM1 in both N_2 and He. These fits were performed using the built-in Levenburg-Marquardt algorithm in MESMER and considered both the experimental measurements performed in this study and the experimental rate coefficients of other groups [5, 9, 10, 17, 20, 23]. These results returned 3.23 ± 0.02 kcal mol^{-1} (*ab initio* value 2.57 kcal mol^{-1}) and 1803 ± 7 cm^{-1} (*ab initio* value 1681cm^{-1}) for the energy and imaginary frequency of TS1 respectively and $\langle \Delta E_{down} \rangle$ for IM1 of 668 ± 20 cm^{-1} and 359 ± 22 cm^{-1} in N_2 and He respectively, with 2σ statistical uncertainties taken from the Leveneburg-Marquardt procedure. These $\langle \Delta E_{down} \rangle$ values are somewhat large, however in the fitting procedure, these parameters are likely taking up uncertainties from other sources, such as the non-fitted Lennard Jones parameters and the use of the harmonic approximation for molecular ro-vibrational densities of states.

The properties of TS1 are particularly well constrained by the lowest pressure experimental rate coefficients of Connell and Howard,[17] and Devolder, *et al.*,[23] since at these pressures, stabilization of IM1 is negligible. A comparison between the experimental data of Connell and Howard,[17] and the MESMER rate coefficients is shown in Figure 10 and the agreement is observed to be excellent. It should be emphasized that the uncertainty on the fitted TS1 parameters is likely much greater than quoted. Firstly both parameters are highly correlated with a correlation coefficient of 0.98 from the fitting procedure and the Levenburg Marquardt errors will not fully account for such correlations. More importantly the fitted values are to some extent model dependent due to the assumption of uncoupled harmonic oscillators when calculating densities of states and the more significant assumption that the vibrational adiabatic potential subject to tunneling may be approximated by the imaginary frequency.

The kinetic behavior of the OH + HNO_3 system can be understood by examining the competition between re-dissociation of IM1 back to OH + HNO_3 (k_{dissoc}) as described in Section 3.3 and the forward reaction from IM1 to IM2 and products via TS1 and TS2 (k_{for}) . Figure 12 shows microcanonical rate coefficients $k_{dissoc}(E)$ and $k_{for}(E)$. Due to entropic considerations k_{dissoc} dominates at high energies, however as the energy approaches the asymptotic limit for re-dissociation back to OH and HNO_3, k_{dissoc} tends to zero and efficient tunneling through TS1 means that k_{for} begins to dominate. The overall rate coefficient for OH loss is controlled by the ratio $\frac{k_{for}}{k_{dissoc}}$ and as the energy (temperature) is reduced, the overall rate coefficient is increased.

These microcanonical arguments also support the explanation of the pressure dependence given in Section 3.3. As the bath gas concentration increases, energy transfer between the bath and IM1 competes with k_{for} and k_{dissoc}, pushing the energy distribution in IM1 towards a Boltzmann distribution. On average this push towards thermalization leads to a net decrease in the energy of IM1, causing the overall rate coefficient to increase and giving rise to the fall off behavior observed both experimentally and theoretically in this work. The high-pressure limiting behavior observed is due to rapid thermalization of IM1 such that a Boltzmann distribution is established in IM1 prior to forward reaction. In this regime the kinetics is well described by the steady state expression:

$$k_{obs} = \frac{k_{assoc}}{k_{dissoc}} k_{for} \qquad \text{(II)}$$

where k_{assoc} and k_{dissoc} are canonical, high-pressure-limiting, rate coefficients for the association of OH + HNO_3 and the reverse dissociation process, whilst k_{for} is the high-pressure rate coefficient for the combined (via both TS1 and TS2) forward reaction from IM1 to IM2.

To complement the master equation calculations, we propose an alternative analytical fitting function to that introduced by Lamb, *et al.*,[21]. If we consider the following scheme:

$$OH + HNO_3 \leftrightarrow IM1^* \quad (6)$$

$$IM1^* + M \leftrightarrow IM1 \quad (7)$$

$$IM1^* \rightarrow H_2O + NO_3 \quad (8)$$

$$IM1 \rightarrow H_2O + NO_3 \quad (9)$$

and following the derivation in the supporting information, we arrive at the following expression:

$$k_1 = \frac{k_6}{k_{-6}} k_8 + \frac{k_6}{k_{-6}} \frac{k_7[M]k_9}{(k_{-7}[M]+k_9)} \quad \text{(III)}$$

These rate coefficients are not thermal quantities since IM1 is always in either an "excited" or "unexcited" state rather than necessarily being in a Boltzmann distribution. However this fitting function does capture the essence of the complex kinetic behavior described in the master equation.

Given the number of fitting parameters and the correlations between them, it was not possible to converge a fit to the experimental data with the newly derived expression (III). When the fit was constrained with fixed parameters (e.g. k_6, k_{-6} and k_7) or with upper/lower bounds, convergence was possible, however the overall fit to the data was worse than when using equation (I). Expansion of this fitting method is beyond the scope of this publication, which aims to provide a reliable method for describing the experimental data herein. Therefore, we present equation (III) as a new and better qualitative method for evaluating k_1 compared to equation (I).

In light of the discussion regarding the pressured dependence of the OH + HNO_3 rate coefficients it is informative to look at the fitting expression (III) in the limit of high and low [M]. At high [M], the fitting expression simplifies to:

$$k_1 = \frac{k_6}{k_{-6}} k_8 + \frac{k_6}{k_{-6}} \frac{k_7[M]k_9}{k_{-7}[M]} \quad \text{(IV)}$$

This expression is broadly equivalent to the steady state expression (II). As [M] tends to zero, (III) simplifies to:

$$k_1 = \frac{k_6}{k_{-6}} k_8 \qquad \text{(V)}$$

Equation (V) demonstrates that even in the absence of collisional stabilization, the transient lifetime of the complex, controlled by k_{-6}, may impact the overall rate. Thus, importantly, the low-pressure limit of the OH + HNO_3 reaction is not equivalent to a bimolecular/transition state theory (TST) type treatment, which would ignore the contribution from the complex. For example, full master equation simulations in the limit of zero pressure at 298 K give an overall rate coefficient of 3.50×10^{-14} cm^3 s^{-1} whereas MESMER calculations of the TST limit (i.e. ignoring IM1) give a rate coefficient of 2.46×10^{-14} cm^3 s^{-1}.

In summary the master equation simulations capture the important features of the kinetics of this system and our results support the observations of Brown, *et al.*,[5] and Gonzalez and Anglada,[31] in demonstrating that the negative temperature dependence to the rate coefficients can be reconciled with a mechanism involving efficient tunneling coupled with a pre-reaction complex similar to that at play in the reaction between OH and methanol at low temperatures [39]. There are, however discrepancies between theory and experiment and more theoretical investigations are needed. Potentially a more accurate description of the vibrational adiabatic potential subject to tunneling potential through TS1 might help reconcile the experimental and theoretical results. Also one aspect of the rate theory, which is yet to be fully explored, is the assumption of ergodicity in the pre-reaction complex. At the energies of the OH + HNO_3 entrance channel IM1 is extremely short lived and any assumptions regarding thermalization (or rapid redistribution of vibrational energy) may not be completely valid, even at the micro-canonical or energy resolved level.

3.5 Atmospheric Modelling

Model simulations were conducted to assess the impact of the new evaluation of the reaction, OH + HNO_3 on OH and NO_x/HNO_3 in the UT-LS were carried out using CRI-STOCHEM (see supplementary material for the details of the modelling set-up). The new kinetic evaluation of the reaction, OH + HNO_3 determined in this study decreases the production of NO_3 or the loss of HNO_3 by 0.21 Tg/yr (32%) and the loss of OH by56.6 Gg/yr (32%) from the base case scenario. These changes have a slight impact on the global budgets of OH, O_3, NO_x, NO_3, HNO_3 by changing their global burdens of -1.2, -0.5, -0.8, -1.2, and 0.2%, respectively. Altering the rate coefficient of OH + HNO_3 reduces the upper tropospheric NO_x, NO_3 and O_3 concentrations, which have the effect of reducing OH concentrations by up to 3% throughout the tropics and southern hemisphere in the upper troposphere (100 hPa) (Figure 13). Because of the decreased loss rate caused by the title reaction, HNO_3 (one of the important NO_y reservoirs) increases up to 3% throughout the tropics in the upper troposphere. The percentage changes of annual nitrogen partitioning (NO_x/HNO_3) relative to the base case integration (Figure 13) reveals a non-negligible reduction of up to 10% in the upper troposphere especially in tropical and southern hemispheric regions. Thus, the new evaluation of the reaction aggravates the disparity between modelled and measured NO_x/HNO_3 reported by Osterman, *et al.*,[1].

4 Conclusion

The bi-molecular rate coefficient for the reaction of OH with HNO_3 has been studied experimentally over the 25 – 750 Torr pressure and 235 – 298 K temperature ranges. The largest uncertainty in the previous measurements of k_1 have been from the [HNO_3] determination, and so

VUV absorption (over 298 – 250 K) was combined with an alternative method for the *in-situ* determination of [HNO_3], which allowed the accurate measurement of k_1 to ± 7% (2σ). The Master Equation calculations presented here highlight the need for further theoretical study into the OH + HNO_3 mechanism and surface, presenting promising results for the future parameterization of this key atmospheric reaction over an extended range of temperatures and pressures. Global modelling studies have shown that, compared to the current k_1 recommendations, the newly determined k_1 have slightly reduced global budgets of key atmospheric species (e.g. OH and O_3) whilst more significant changes in the NO_x/HNO_3 ratio (-10%) were observed in the tropical upper troposphere regions.

Conflicts of Interest

There are no conflicts to declare.

Acknowledgements

The experimental research was carried out by the Jet Propulsion Laboratory, California Institute of Technology, under contract with the National Aeronautics and Space Administration (NASA), and was supported by the Upper Atmosphere Research Program. Frank Winiberg's research was supported by an appointment to the NASA Postdoctoral Program, administered by Universities Space Research Association under contract with NASA. We thank NERC (grant code-NE/K004905/1) and Bristol ChemLabS under whose auspices various aspects of this work was funded. Funding for RJS was provided by the US Air Force Office of Scientific Research (AFOSR)

under Contract No. FA9550-16-1-0051 and a researcher mobility grant from the Royal Society of Chemistry.

5 Figures

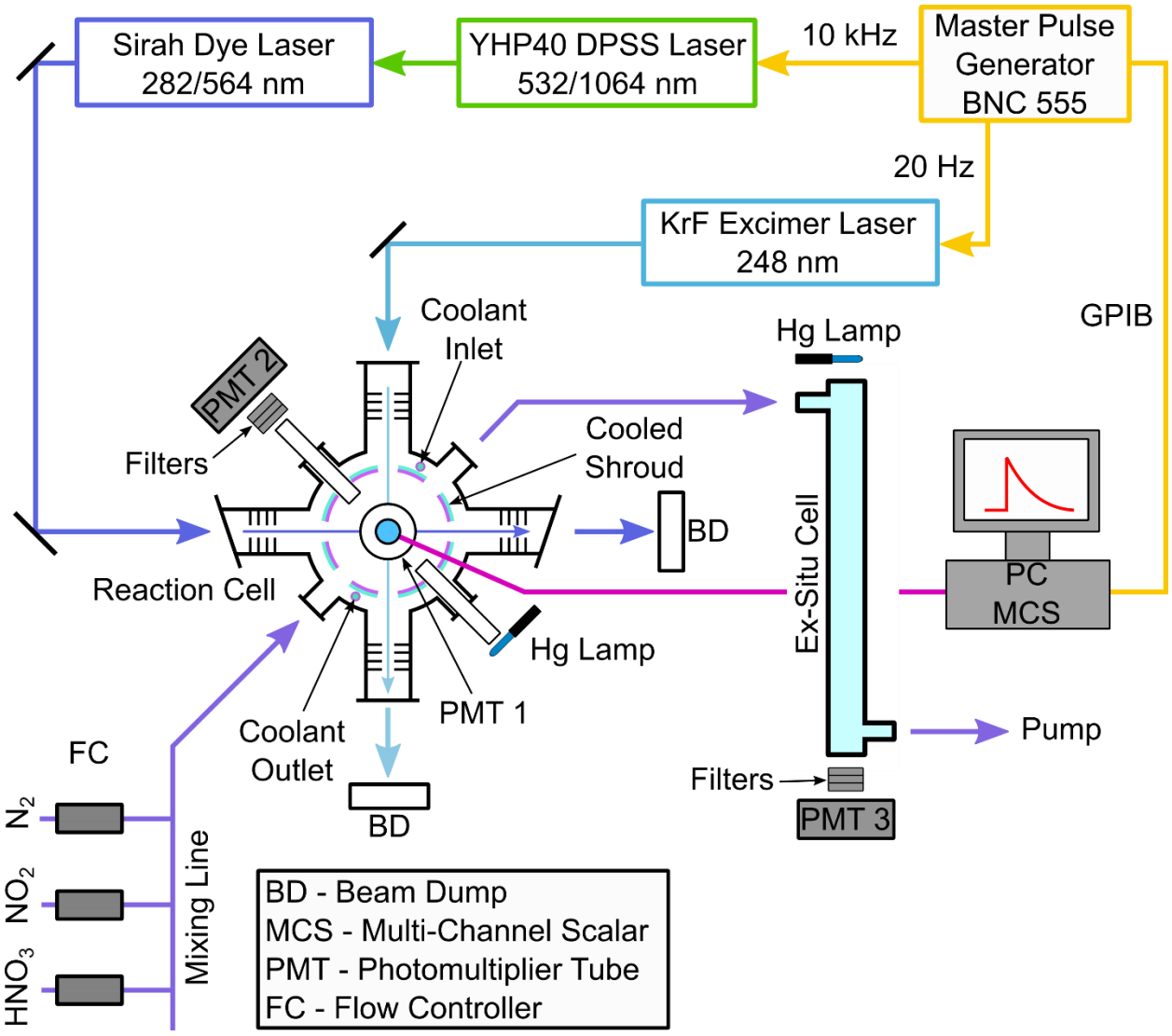

Figure 1: Schematic of the PLP-LIF system.

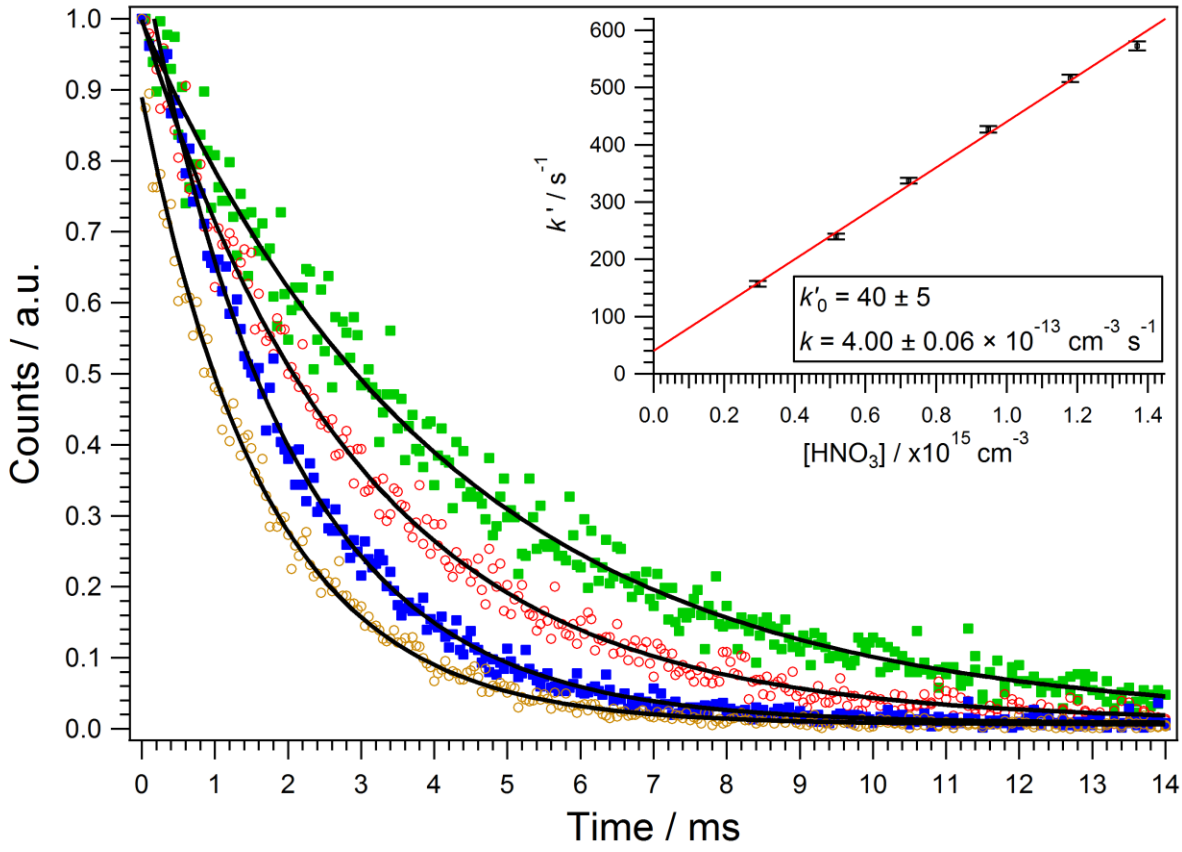

Figure 2: OH decay profiles recorded at 200 Torr and 235 K ([HNO_3] = 0.3 – 1.4 × 10^{15} cm^{-3}), fit with a single exponential decay to determine *k*'. The inset figure shows the rate coefficient determination for the same experiment by plotting *k*' against the [HNO_3] measured using the in-situ 2*hv* PIF method. Error bars represent the total fit uncertainty to ±2σ.

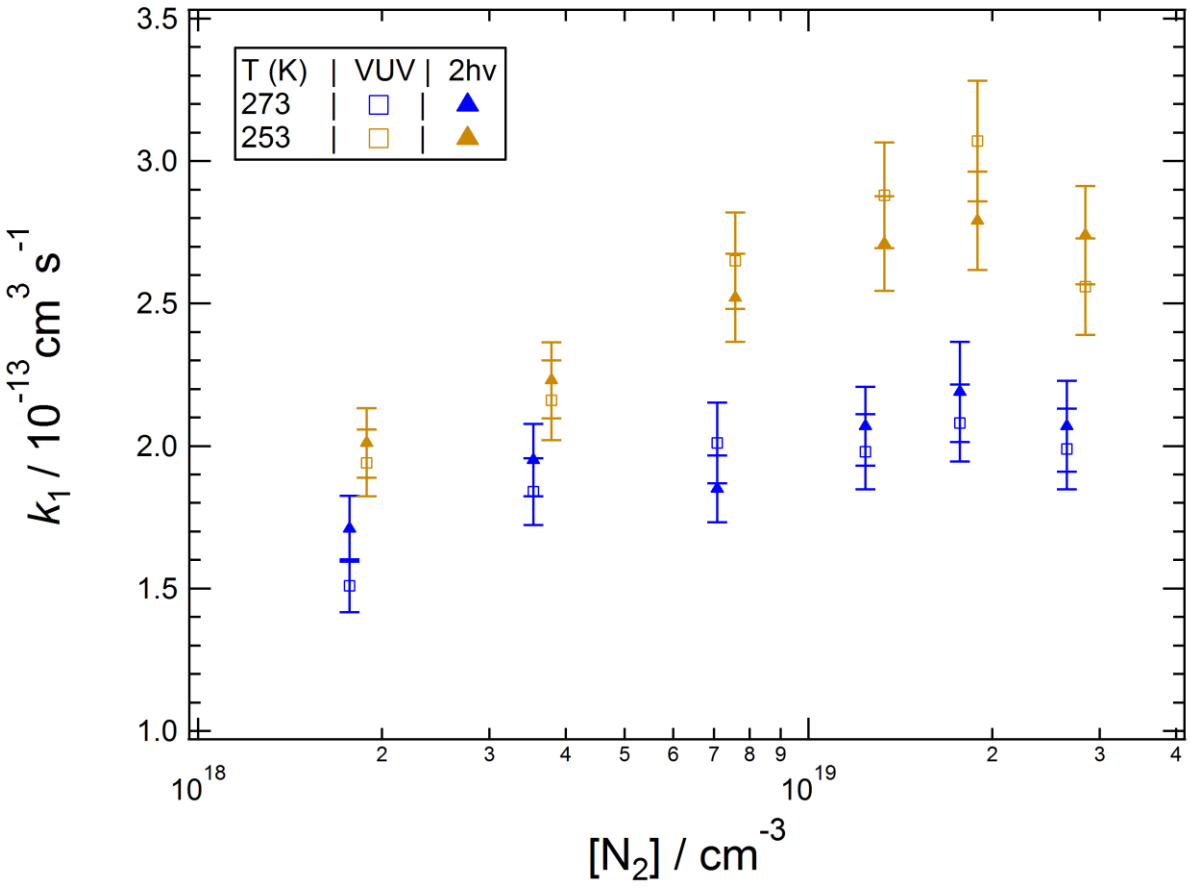

Figure 3: Comparison of k_1 as a function of bath gas concentration, derived using the VUV and 2-photon PIF methods of [HNO_3] determination. Rate coefficients were measured simultaneously using both methods at 273 and 253 K, over a 50 – 750 Torr pressure range. Each data point represents the weighted average of 3 or more measurements and the error bars represent the total uncertainty in the measured rate coefficient to ±2σ.

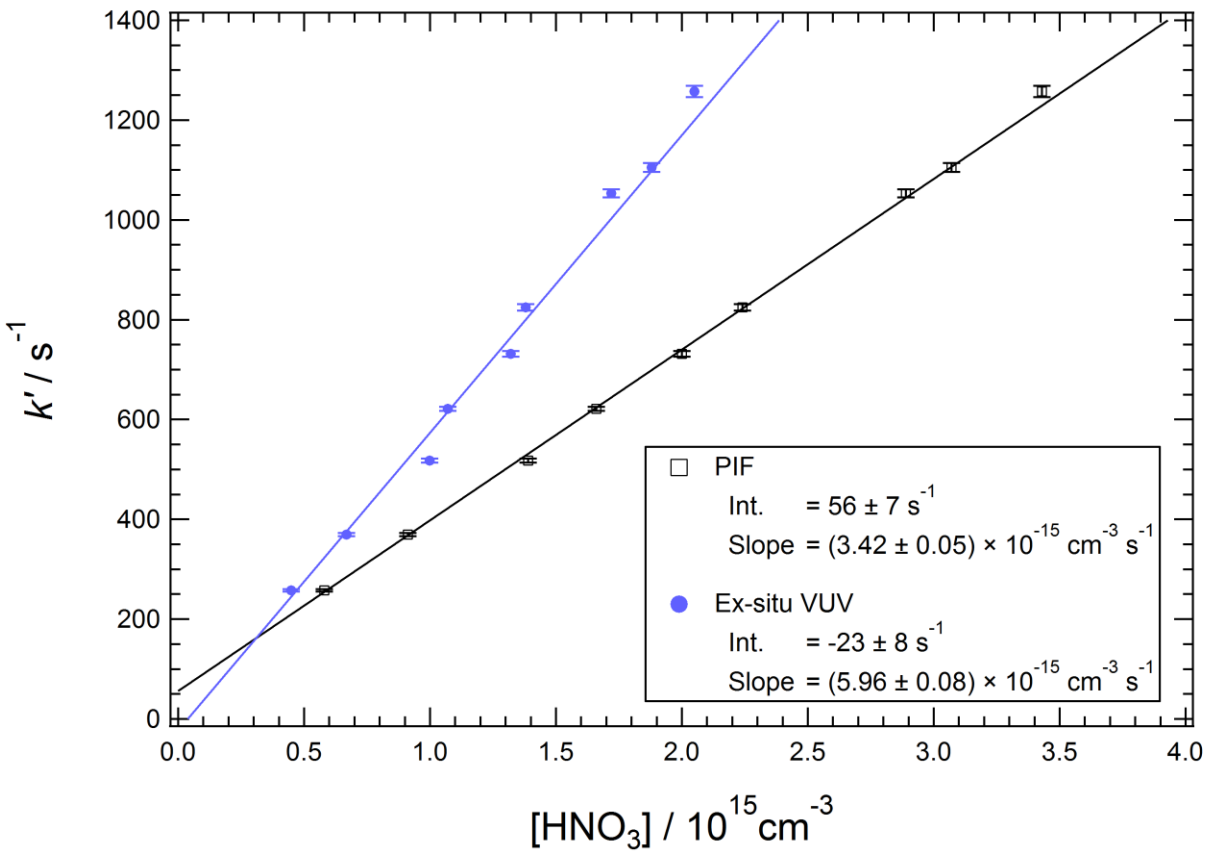

Figure 4: Pseudo-first order rate coefficient, *k*', as a function of [HNO_3] determined using the PIF and ex-situ VUV detection methods at 235 K and 200 Torr. Error bars represent the fit parameter uncertainty (±2σ) and the quoted parameters uncertainties are quoted to ±2σ.

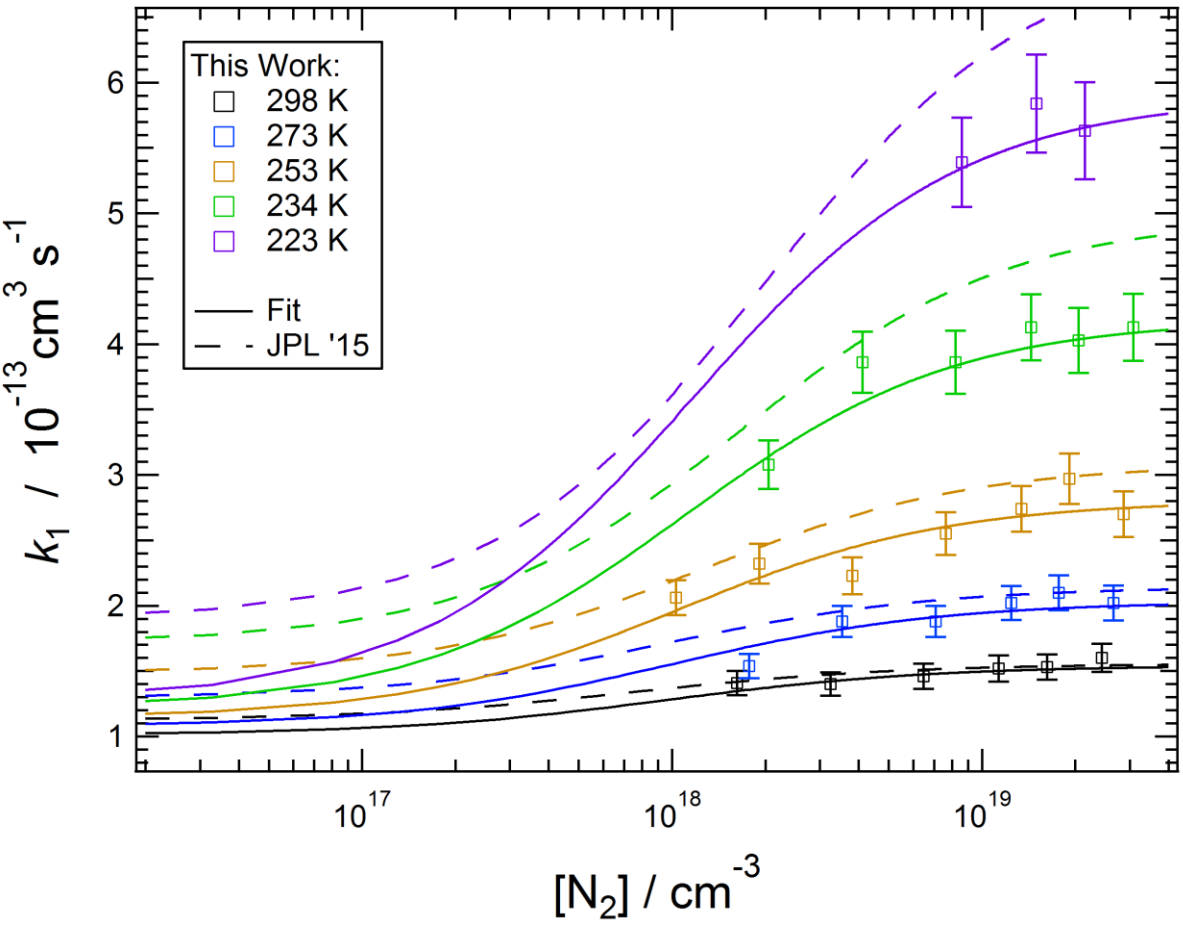

Figure 5. Bimolecular rate coefficient, k_1, as a function of bath gas pressure (25 – 750 Torr) over the 223 – 298 K temperature range. Each data point represents the weighted average of 3 or more measurements and the error bars represent the total uncertainty in the measured rate coefficient to ±2σ. Weighted fit to the data shown, using the function described in Lamb, *et al.*,[21], including low P literature data from Connell and Howard,[17]. JPL-2015 recommended fits shown for comparison [19].

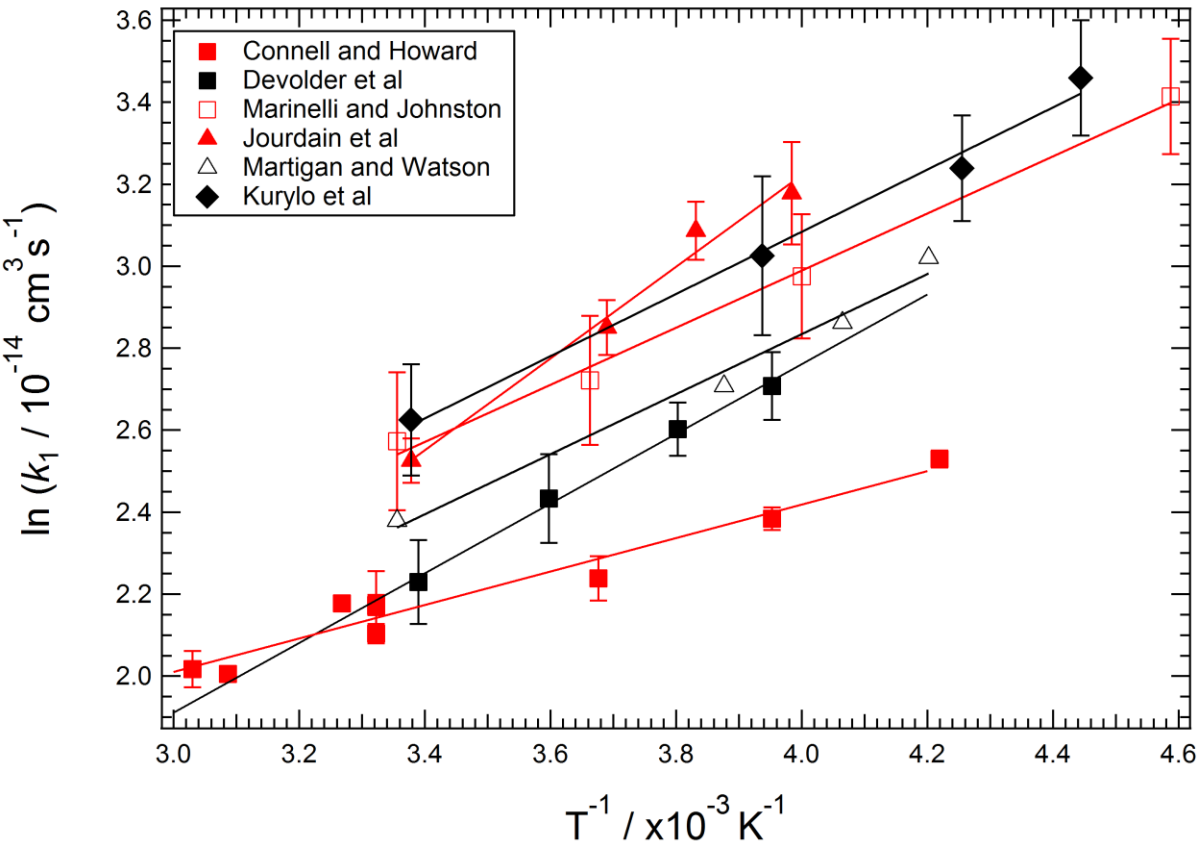

Figure 6: Comparison of literature values for experimentally obtained rate coefficients for reaction (1) at 10 Torr or below as a function of 1/*T*. References: [8, 17, 22-25].

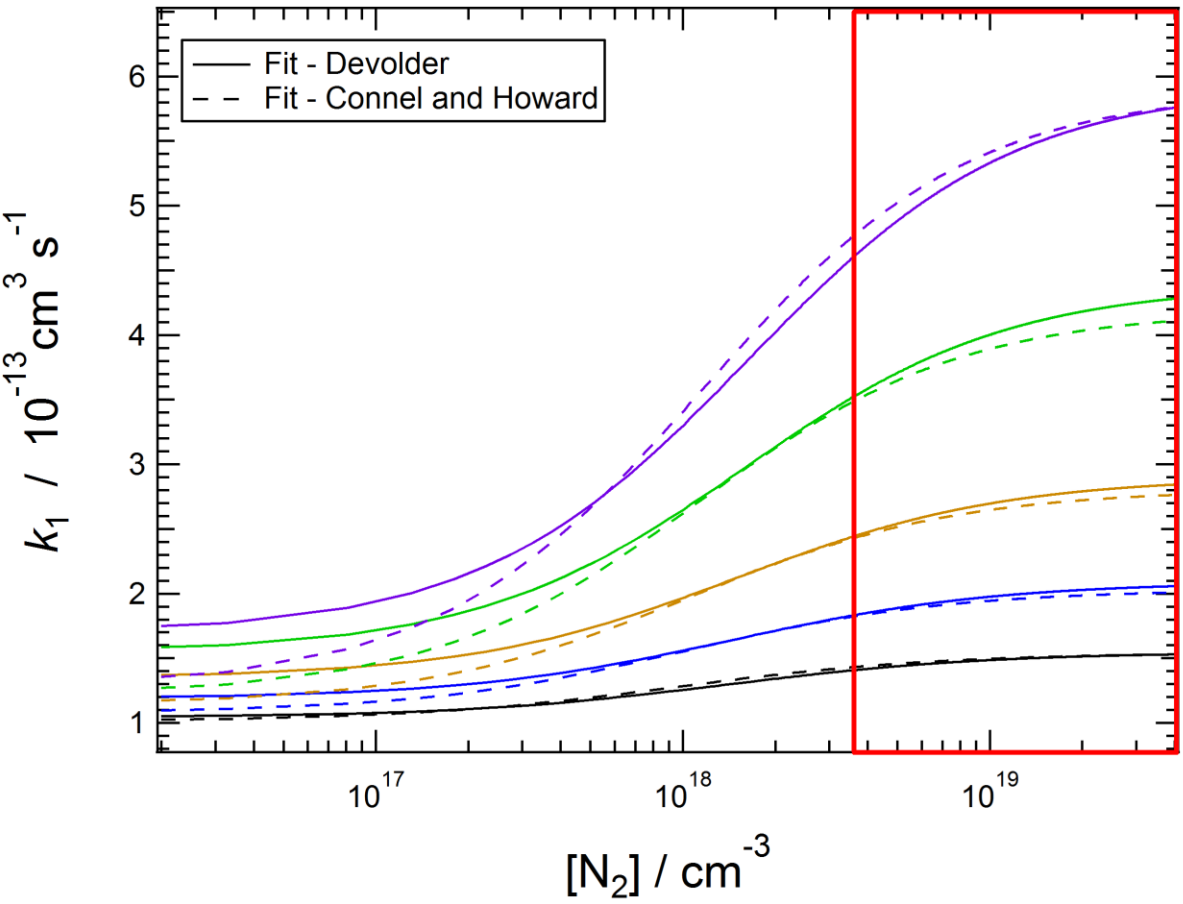

Figure 7: Comparison of the fit to our data, using equation (I), constraining the low pressure fit with both the Devolder, *et al.*,[23] and the Connell and Howard,[17] Arrhenius expressions. The uncertainties in the given Arrhenius expressions were used to weight the fits towards the low pressure limit. Colors represent the temperatures used in figure 5. Red highlighted area represents pressures important in the lowest ~16 km of the atmosphere.

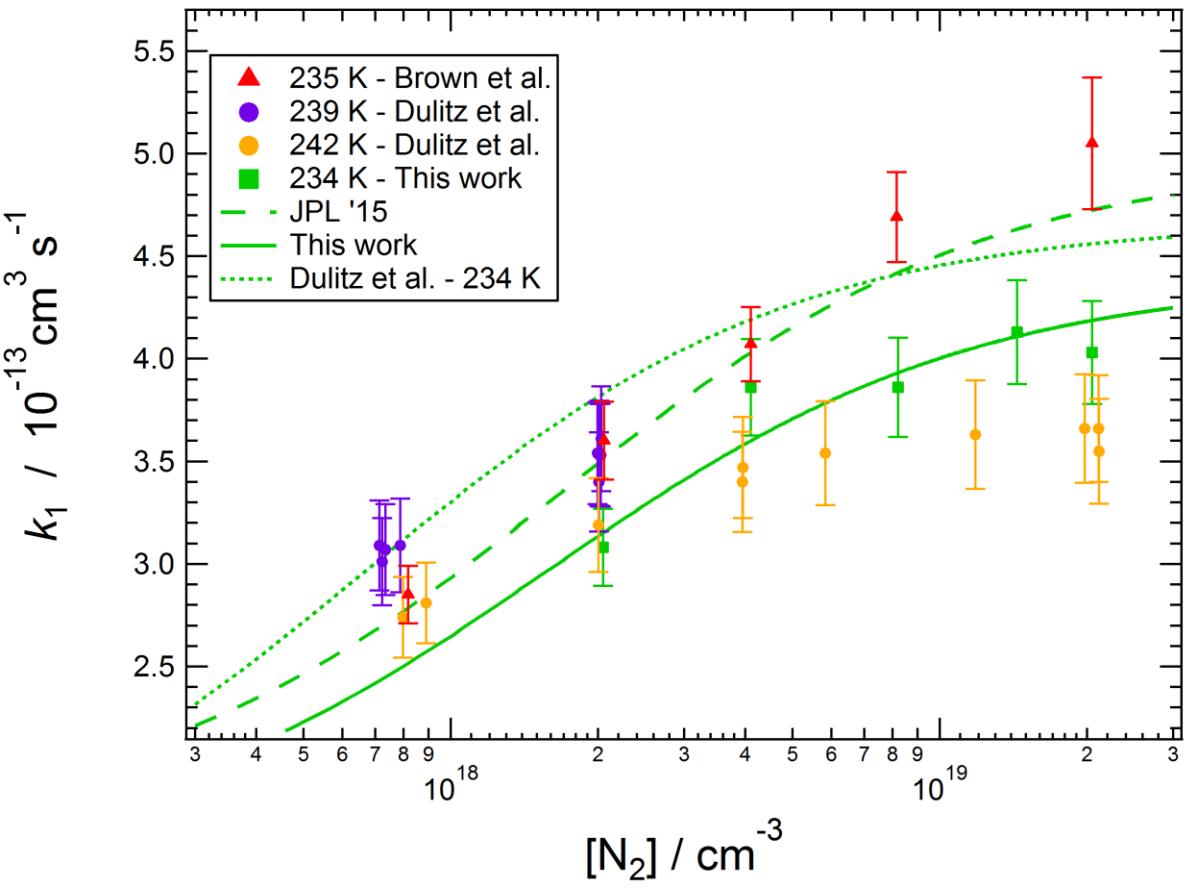

Figure 8: Comparison of the fit parameters from this work with Burkholder, *et al.*,[19] and Dulitz, *et al.*,[10] calculated at 235K using equation (I). Also shown are the experimental data points from this work and Brown, *et al.*,[5] at 235 K, and experimental data from Dulitz, *et al.*,[10] at the closest representative temperatures (239 and 242 K). Data points were used from Brown, *et al.*,[5] with reported uncertainties - ~7% uncertainty was added to the points from Dulitz, *et al.*,[10], in line with their reported systematic uncertainties.

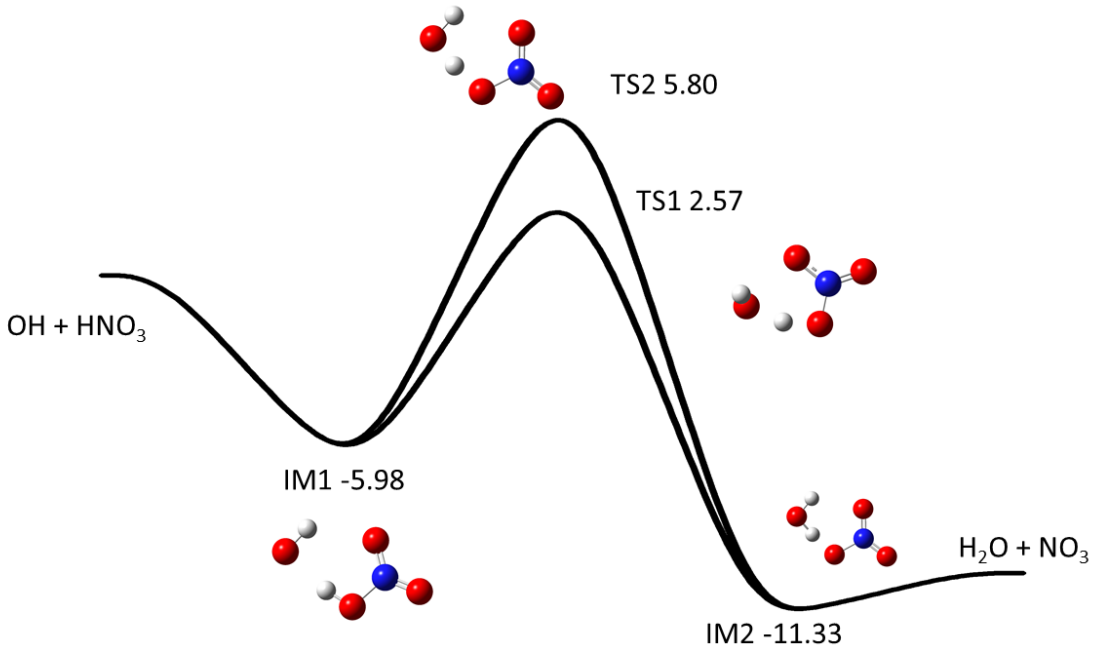

Figure 9: Schematic potential energy surface for the OH + HNO_3 reaction from calculations at the M062x/6-311+G(3d,2p)//ROHF-UCCSD(T)-f12b/aug-cc-pvTZ level of theory. All energies are given in kcal mol^{-1} relative to OH + HNO_3

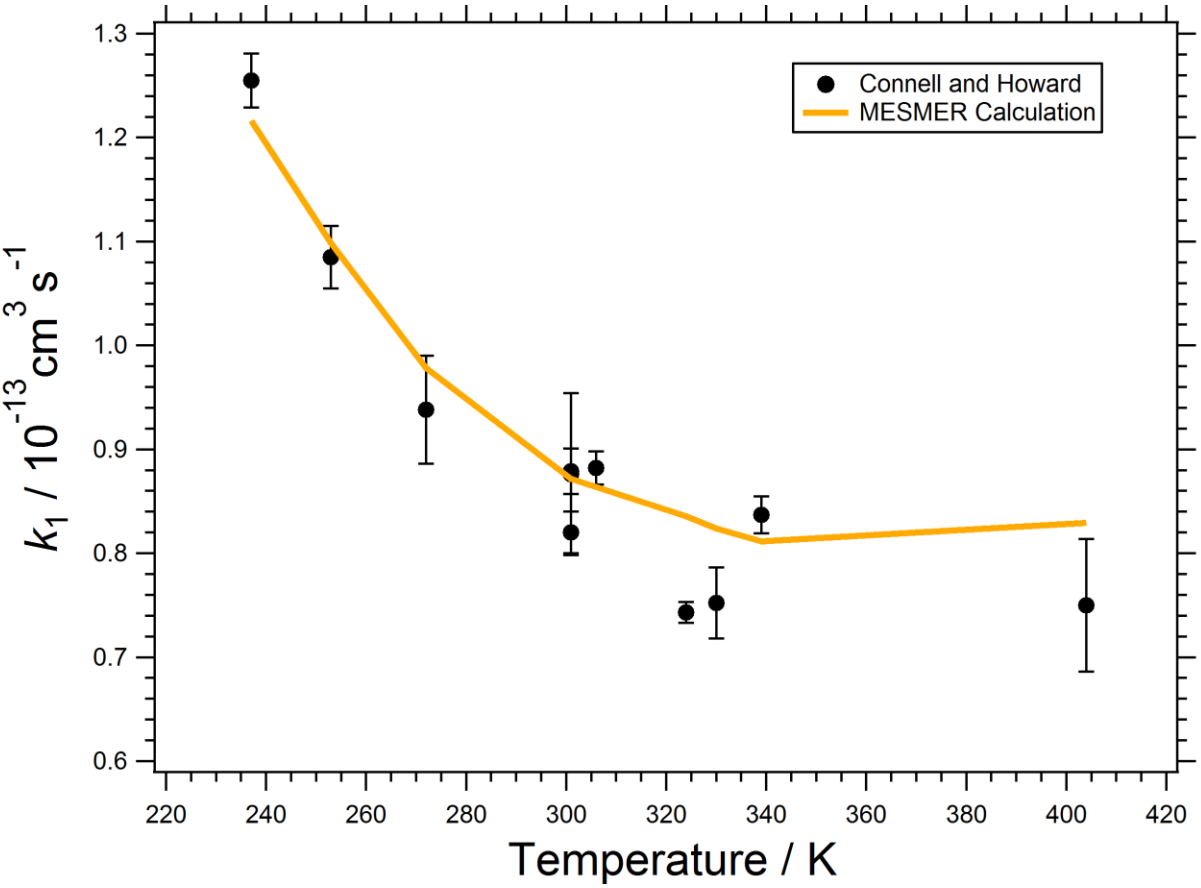

Figure 10: Comparison between theoretical rate coefficients calculated using the optimized master equation model in MESMER and experimental low pressure rate coefficients measured by Connell and Howard,[17].

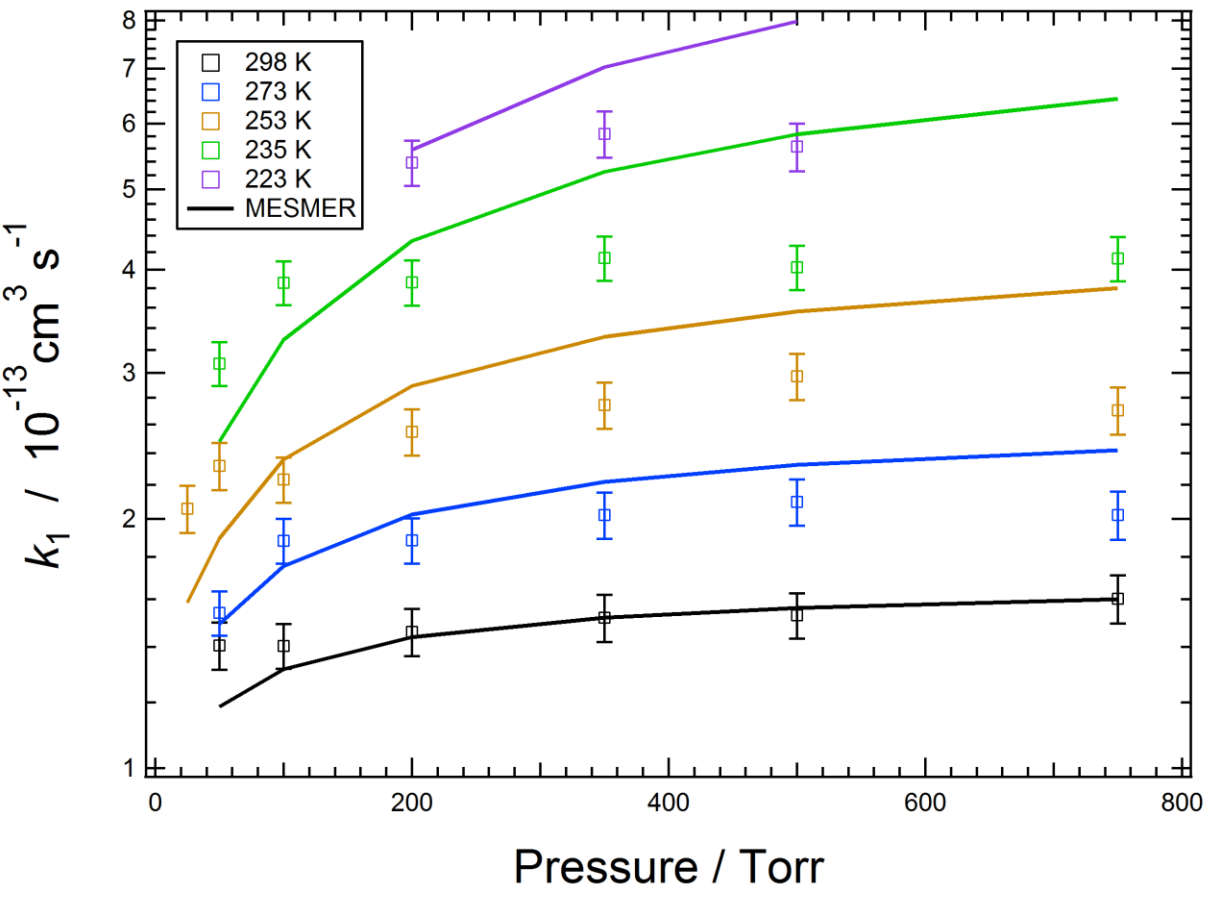

Figure 11: Comparison between theoretical rate coefficients calculated using the optimized master equation model in MESMER and experimental pressure dependent rate coefficients measured in the current work. The y-axis is a logarithmic scale.

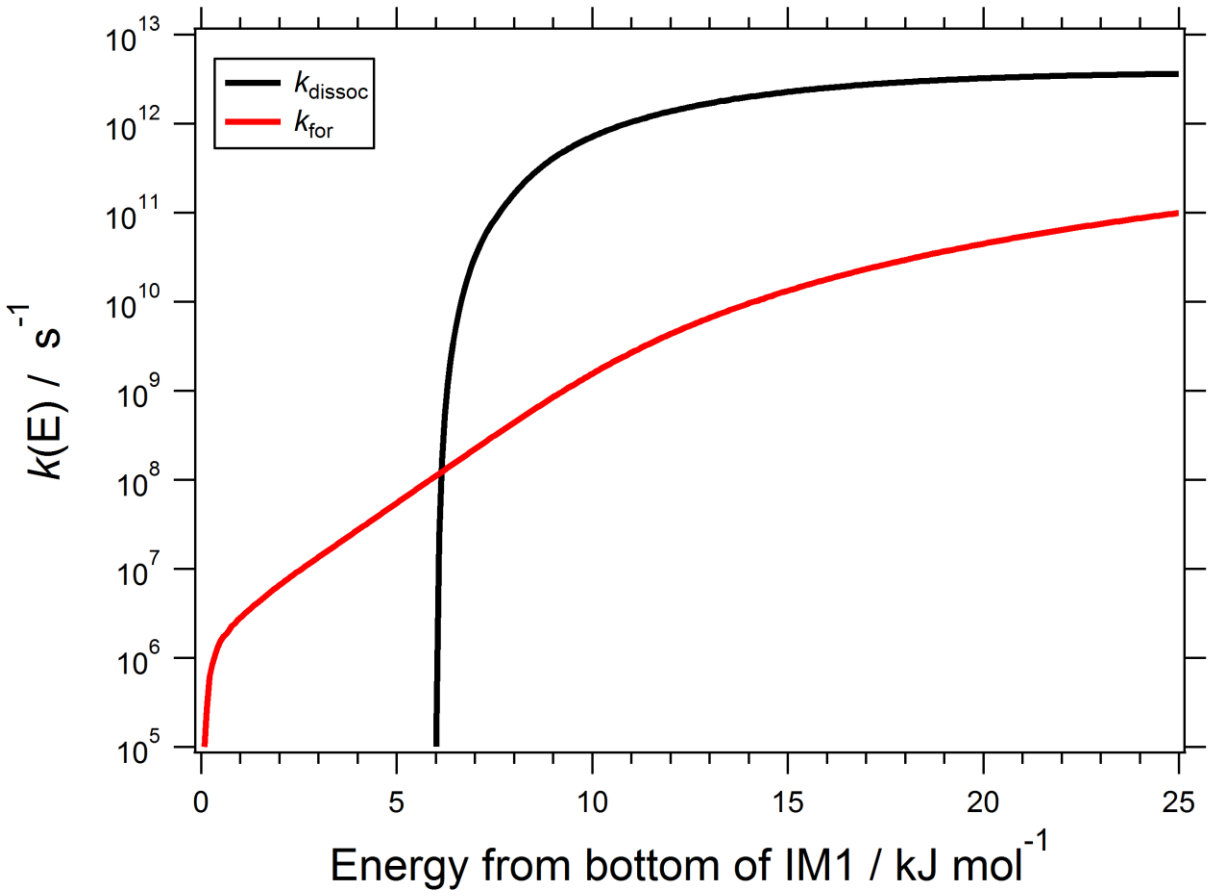

Figure 12: Microcanonical rate coefficients $k_{dissoc}(E)$ and $k_{for}(E)$ (for simplicity, k_{for} in this plot only considers reaction via TS1 since this is the dominant channel).

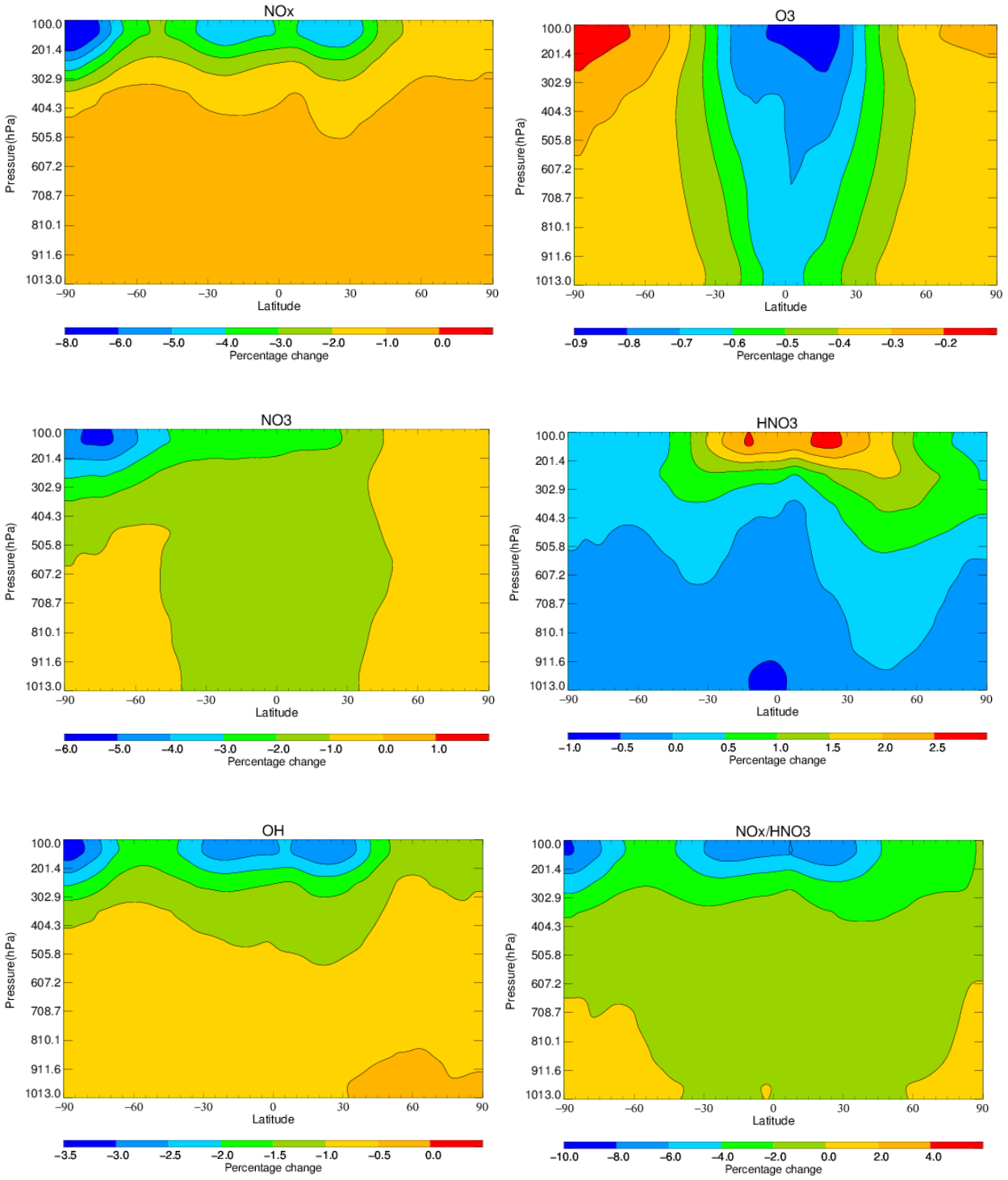

Figure 13: Annual zonal percentage changes in NO_x, O_3, NO_3, HNO_3, OH and NO_x/HNO_3 after altering the rate coefficient of the title reaction in base case scenario.

6 Tables

Temp (K)	Pressure (Torr)	k_1 ($\times 10^{-13}$ cm^3 s^{-1})	# of measurements
298	50	1.41 ± 0.04	3
	100	1.40 ± 0.02	4
	200	1.46 ± 0.04	6
	350	1.52 ± 0.04	6
	500	1.53 ± 0.03	5
	750	1.60 ± 0.05	3
273	50	1.54 ± 0.02	5
	100	1.88 ± 0.03	8
	200	1.88 ± 0.03	5
	350	2.02 ± 0.05	7
	500	2.10 ± 0.05	6
	750	2.02 ± 0.06	3
253	25	2.06 ± 0.03	6
	50	2.32 ± 0.04	6
	100	2.23 ± 0.01	10
	200	2.55± 0.03	10
	350	2.74 ± 0.03	8
	500	2.97 ± 0.04	9
	750	2.70 ± 0.04	10
234	50	3.08 ± 0.03	3
	100	3.86 ± 0.04	5
	200	3.86 ± 0.07	5
	350	4.13 ± 0.06	3
	500	4.03 ± 0.06	3
	750	4.13 ± 0.06	2
223	200	5.39 ± 0.11	2
	350	5.84 ± 0.14	2
	500	5.63 ± 0.15	2

Table 1: Observed rate coefficients for the reaction of OH + HNO_3 over a range of pressures (25 – 750 Torr) and temperatures (223 – 298 K). The uncertainty associated with the rate coefficients is given at the two standard deviation level from a 95% confidence limit linear least squares routine fit of the second order plot.

Source	A_0 10^{-14} cm^3 s	Ea_0 K	A_3 10^{-17} cm^3 s	Ea_3 K	A_2 10^{-34} cm^3 s	Ea_2 K
JPL-15[a]	2.40	450	2.70	2200	6.50	1335
Fit	3.1 (1.7)	420 (190)	4.8 (4.5)	2000 (200)	0.002 (0.016)	3100 (1600)
Fit (Dev)[b]	2.2 (0.9)	500 (130)	3.0 (2.7)	2120 (190)	0.1 (0.6)	2180 (210)
Fit (Con)[c]	5.2 (3.4)	200 (220)	8.4 (7.6)	1900 (190)	1.6 (6.3)	1745 (640)

Table 2: Derived fit variables for the k_0, k_Δ and k_c used in the Troe expression (I) global fit to the data across the full pressure and temperature range. *A* and *Ea* variables are used in Arrhenius type expressions, where $k_0 = A_0 \times \exp(-Ea_0/T)$. Uncertainties in parentheses quoted to ±1σ. [a] – Burkholder, *et al.*,[19]; [b,c] – Global fit included low pressure data from literature sources Devolder, *et al.*,[23] and Connell and Howard,[17] respectively.

Component	Value	% VUV	% two-photon
[HNO_3] (2hv method)		**6**	**6**
- σ_{HNO3} / cm^2	$(1.6 \pm 0.1) \times 10^{-17}$	6	6
- Decay fit / s^{-1}			1-2
- Pathlength / cm	10.9 ± 0.2	2	
Temperature / K	± 2	**1-2**	**1-2**
Total		**7**	**7**

Table 3: Percentage systematic uncertainty in the measured $k_{OH+HNO3}$ rate coefficients. Uncertainty in the VUV and two photon determination of [HNO_3] shown for comparison. Total uncertainty calculated as the sum-in-quadrature of the individual uncertainties.

References

1. G. B. Osterman, B. Sen, G. C. Toon, R. J. Salawitch, J. J. Margitan, J. F. Blavier, D. W. Fahey and R. S. Gao, *Geophys. Res. Lett.*, 1999, **26**, 1157-1160.
2. H. B. Singh, Y. Chen, G. L. Gregory, G. W. Sachse, R. Talbot, D. R. Blake, Y. Kondo, J. D. Bradshaw, B. Heikes and D. Thornton, *Geophys. Res. Lett.*, 1997, **24**, 127-130.
3. G. Berthet, N. Huret, F. Lefèvre, G. Moreau, C. Robert, M. Chartier, V. Catoire, B. Barret, I. Pisso and L. Pomathiod, *Atmos. Chem. Phys.*, 2006, **6**, 1599-1609.
4. D. A. Hauglustaine, B. A. Ridley, S. Solomon, P. G. Hess and S. Madronich, *Geophys. Res. Lett.*, 1996, **23**, 2609-2612.
5. S. S. Brown, R. K. Talukdar and A. R. Ravishankara, *J. Phys. Chem. A*, 1999, **103**, 3031-3037.
6. R. S. Gao, D. W. Fahey, L. A. Del Negro, S. G. Donnelly, E. R. Keim, J. A. Neuman, E. Teverovskaia, P. O. Wennberg, T. F. Hanisco, E. J. Lanzendorf, M. H. Proffitt, J. J. Margitan, J. C. Wilson, J. W. Elkins, R. M. Stimpfle, R. C. Cohen, C. T. McElroy, T. P. Bui, R. J. Salawitch, S. S. Brown, A. R. Ravishankara, R. W. Portmann, M. K. W. Ko, D. K. Weisenstein and P. A. Newman, *Geophys. Res. Lett.*, 1999, **26**, 1153-1156.
7. D. J. Lary, D. E. Shallcross and R. Toumi, *Journal of Geophysical Research: Atmospheres*, 1999, **104**, 15929-15940.
8. J. J. Margitan and R. T. Watson, *J. Phys. Chem.*, 1982, **86**, 3819-3824.
9. R. A. Stachnik, L. T. Molina and M. J. Molina, *J. Phys. Chem.*, 1986, **90**, 2777-2780.
10. K. Dulitz, D. Amedro, T. J. Dillon, A. Pozzer and J. N. Crowley, *Atmos. Chem. Phys. Discuss.*, 2017, **2017**, 1-29.
11. B. Newsome and M. Evans, *Atmos. Chem. Phys.*, 2017, **17**, 14333-14352.
12. A. K. Mollner, S. Valluvadasan, L. Feng, M. K. Sprague, M. Okumura, D. B. Milligan, W. J. Bloss, S. P. Sander, P. T. Martien, R. A. Harley, A. B. McCoy and W. P. L. Carter, *Science*, 2010, **330**, 646-649.
13. Y. D. Liu and S. P. Sander, *J. Phys. Chem. A*, 2015, **119**, 10060-10066.
14. F. A. F. Winiberg, C. J. Percival and S. Sander, *In preparation*, 2018.
15. F. Biaume, *J. Photochem.*, 1973, **2**, 139-149.
16. P. H. Wine, A. R. Ravishankara, N. M. Kreutter, R. C. Shah, J. M. Nicovich, R. L. Thompson and D. J. Wuebbles, *J. Geophys. Res.*, 1981, **86**, 1105-1112.
17. P. S. Connell and C. J. Howard, *Int. J. Chem. Kinet.*, 1985, **17**, 17-31.
18. R. D. Kenner, F. Rohrer, T. Papenbrock and F. Stuhl, *The Journal of Physical Chemistry*, 1986, **90**, 1294-1299.
19. J. B. Burkholder, S. P. Sander, J. Abbatt, J. R. Barker, R. E. Huie, C. E. Kolb, M. J. Kurylo, V. L. Orkin, D. M. Wilmouth and P. H. Wine, *Chemical Kinetics Data for Use in Atmospheric Studies: Evaluation No. 18*, Report 15-10, Jet Propulsion Laboratory, Pasadena, 2015.
20. S. S. Brown, J. B. Burkholder, R. K. Talukdar and A. R. Ravishankara, *J. Phys. Chem. A*, 2001, **105**, 1605-1614.
21. J. J. Lamb, M. Mozurkewich and S. W. Benson, *The Journal of Physical Chemistry*, 1984, **88**, 6441-6448.
22. J. L. Jourdain, G. Poulet and G. Le Bras, *J. Chem. Phys.*, 1982, **76**, 5827-5833.
23. P. Devolder, M. Carlier, J. F. Pauwels and L. R. Sochet, *Chem. Phys. Lett.*, 1984, **111**, 94-99.

24. W. J. Marinelli and H. S. Johnston, *J. Chem. Phys.*, 1982, **77**, 1225-1234.
25. M. J. Kurylo, K. D. Cornett and J. L. Murphy, *J. Geophys. Res.* , 1982, **87**, 3081-3085.
26. J. V. Seeley, J. T. Jayne and M. J. Molina, *Int. J. Chem. Kinet.*, 1993, **25**, 571-594.
27. J. R. Barker and D. M. Golden, *Chem. Rev.*, 2003, **103**, 4577-4591.
28. J. A. Miller and S. J. Klippenstein, *J. Phys. Chem. A*, 2003, **107**, 2680-2692.
29. M. J. Pilling and S. H. Robertson, *Annu. Rev. Phys. Chem.*, 2003, **54**, 245-275.
30. W. S. Xia and M. C. Lin, *J. Chem. Phys.*, 2001, **114**, 4522-4532.
31. J. Gonzalez and J. M. Anglada, *J. Phys. Chem. A*, 2010, **114**, 9151-9162.
32. R. D. Gaussian 09, M. J. Frisch, G. W. Trucks, H. B. Schlegel, G. E. Scuseria, M. A. Robb, J. R. Cheeseman, G. Scalmani, V. Barone, B. Mennucci, G. A. Petersson, H. Nakatsuji, M. Caricato, X. Li, H. P. Hratchian, A. F. Izmaylov, J. Bloino, G. Zheng, J. L. Sonnenberg, M. Hada, M. Ehara, K. Toyota, R. Fukuda, J. Hasegawa, M. Ishida, T. Nakajima, Y. Honda, O. Kitao, H. Nakai, T. Vreven, J. J. A. Montgomery, J. E. Peralta, F. Ogliaro, M. Bearpark, J. J. Heyd, E. Brothers, K. N. Kudin, V. N. Staroverov, T. Keith, R. Kobayashi, J. Normand, K. Raghavachari, A. Rendell, J. C. Burant, S. S. Iyengar, J. Tomasi, M. Cossi, N. Rega, J. M. Millam, M. Klene, J. E. Knox, J. B. Cross, V. Bakken, C. Adamo, J. Jaramillo, R. Gomperts, R. E. Stratmann, O. Yazyev, A. J. Austin, R. Cammi, C. Pomelli, J. W. Ochterski, R. L. Martin, K. Morokuma, V. G. Zakrzewski, G. A. Voth, P. Salvador, J. J. Dannenberg, S. Dapprich, A. D. Daniels, O. Farkas, J. B. Foresman, J. V. Ortiz, J. Cioslowski, D. J. Fox, I. Gaussian and W. CT, *Journal*, 2013.
33. H. J. Werner, G. Knizia and F. R. Manby, *Mol. Phys.*, 2011, **109**, 407-417.
34. H. J. Werner, P. J. Knowles, G. Knizia, F. R. Manby and M. Schutz, *Wiley Interdiscip. Rev.-Comput. Mol. Sci.*, 2012, **2**, 242-253.
35. D. R. Glowacki, C. H. Liang, C. Morley, M. J. Pilling and S. H. Robertson, *J. Phys. Chem. A*, 2012, **116**, 9545-9560.
36. S. H. Robertson, M. J. Pilling, D. L. Baulch and N. J. B. Green, *J. Phys. Chem.*, 1995, **99**, 13452-13460.
37. D. C. McCabe, S. S. Brown, M. K. Gilles, R. K. Talukdar, I. W. M. Smith and A. R. Ravishankara, *J. Phys. Chem. A*, 2003, **107**, 7762-7769.
38. S. Sharma, S. Raman and W. H. Green, *J. Phys. Chem. A*, 2010, **114**, 5689-5701.
39. R. J. Shannon, M. A. Blitz, A. Goddard and D. E. Heard, *Nat Chem*, 2013, **5**, 745-749.